Subduction Zone Interface Structure within the Southern MW9.2 1964 Great Alaska Earthquake Asperity: Constraints from Receiver Functions Across a Spatially Dense Node Array

Evans Awere Onyango[1,1], Lindsay L. Worthington[1,1], Brandon Schmandt[1,1], and Geoffrey A. Abers[2,2]

[1]University of New Mexico
[2]Cornell University

November 30, 2022

Abstract

We conduct a high-resolution teleseismic receiver function investigation of the subducting plate interface within the Alaskan forearc beneath Kodiak Island using data collected as part of the Alaska Amphibious Community Seismic Experiment in 2019. The Kodiak node array consisted of 398 nodal geophones deployed at ˜200-300 m spacing on northeastern Kodiak Island within the southern asperity of the 1964 Mw9.2 Great Alaska earthquake. Receiver function images at frequencies of 1.2 and 2.4 Hz show a coherent, slightly dipping velocity increase at ˜30-40 km depth consistent with the expected slab Moho. In contrast to studies within the northern asperity of the 1964 rupture, we find no evidence for a prominent low-velocity layer above the slab Moho thick enough to be resolved by upgoing P-to-S conversions. These results support evidence from seismicity and geodetic strain suggesting that the 1964 rupture connected northern (Kenai) and southern (Kodiak) asperities with different plate interface properties.

Title: Subduction Zone Interface Structure within the Southern M_W9.2 1964 Great Alaska Earthquake Asperity: Constraints from Receiver Functions Across a Spatially Dense Node Array

Authors: Evans A. Onyango[1*], Lindsay L. Worthington[1], Brandon Schmandt[1], Geoffrey Abers[2]

***Corresponding Author:**

Evans A. Onyango, eaonyango@unm.edu

Department of Earth and Planetary Sciences, Northrop Hall, 221 Yale Blvd NE, University of New Mexico, Albuquerque, New Mexico 87131, USA.

Affiliations:

[1]Department of Earth and Planetary Sciences, Northrop Hall, 221 Yale Blvd NE, University of New Mexico, Albuquerque, New Mexico 87131, USA.

[2]Department of Earth and Atmospheric Sciences, Cornell University, 112 Hollister Drive, Ithaca, NY, 14853-1504, USA.

Key Points:

- We present receiver function imaging from a dense three-component nodal array deployment on Kodiak Island above the subducting Pacific Plate.
- A clear slab Moho conversion is found but, in contrast to the Kenai Peninsula, there is no coherent low-velocity layer atop the slab.
- The 1964 Great Alaska Earthquake ruptured across structural segments with different plate interface properties.

Abstract

We conduct a high-resolution teleseismic receiver function investigation of the subducting plate interface within the Alaskan forearc beneath Kodiak Island using data collected as part of the Alaska Amphibious Community Seismic Experiment in 2019. The Kodiak node array consisted of 398 nodal geophones deployed at ~200-300 m spacing on northeastern Kodiak Island within the southern asperity of the 1964 Mw9.2 Great Alaska earthquake. Receiver function images at frequencies of 1.2 and 2.4 Hz show a coherent, slightly dipping velocity increase at ~30-40 km depth consistent with the expected slab Moho. In contrast to studies within the northern asperity of the 1964 rupture, we find no evidence for a prominent low-velocity layer above the slab Moho thick enough to be resolved by upgoing P-to-S conversions. These results support evidence from seismicity and geodetic strain suggesting that the 1964 rupture connected northern (Kenai) and southern (Kodiak) asperities with different plate interface properties.

Plain Language Summary

We use 398 portable seismometers that were deployed as part of the Alaska Amphibious Community Seismic Experiment to image the boundary between the subducting Pacific plate and the base of the North American plate. The seismometers, spaced ~200-300 m apart, were stationed on Kodiak Island in 2019 within the southern rupture area of the 1964 Mw9.2 Great Alaska earthquake. We analyze conversions from compressional to shear waves from distant earthquakes to understand the conditions of the plate interface. Our results show a dipping velocity increase at ~30-40 km depth at the expected location of the Pacific slab crust-mantle boundary. In contrast to prior results from the northern 1964 rupture zone, we do not find a low-

46 velocity layer on the subducting plate. Our results indicate that the 1964 rupture connected
47 segments of the Alaskan subduction zone with different plate interface properties.

48 **1 Introduction**

49 Understanding plate interface structure and subduction geometries can illuminate slip
50 mechanisms, earthquake rupture behavior and shallow subduction zone processes. Because most
51 global forearc regions are submerged, they are commonly studied via marine seismic methods,
52 which, thus far, precludes dense-array natural source seismic imaging. Therefore, well-exposed
53 forearcs such as Kodiak Island provide rare opportunities to study subduction zone and plate
54 interface structure within the shallow forearc using a dense seismic array. Here, we use three-
55 component node array data acquired in 2019 across northeastern Kodiak Island as part of the
56 Alaska Amphibious Community Seismic Experiment (AACSE) to compute Ps teleseismic
57 receiver functions (RFs) to better understand the nature of the plate interface in the rupture area
58 of the 1964 Mw9.2 Great Alaska earthquake.

59 The Alaska-Aleutian subduction zone has hosted more M>8 earthquakes than any other
60 system globally and offers opportunities to explore relationships between megathrust slip
61 phenomena, seismicity, deformation and forearc structure. The Kodiak node array (Fig. 1a-c) lies
62 within the southern rupture area of the 1964 Mw9.2 Great Alaska earthquake, the second largest
63 earthquake ever recorded (Kanamori, 1977, Fig. 1a). Coseismic slip and ground shaking from
64 this event created damage across a 600-800 km section of the Alaskan margin and triggered local
65 and far-field tsunami. Previous work investigating static deformation, seismic waves, and
66 tsunami propagation from this event revealed two major coseismic slip asperities: the Kenai
67 asperity in the north and the Kodiak asperity in the south (Christensen & Beck, 1994; Ichinose et
68 al., 2007; Johnson et al., 1996; Suito & Freymueller, 2009; Fig. 1a). Differences in coseismic slip

(Johnson et al., 1996), major earthquake recurrence interval (Wesson et al., 1999; Nishenko and Jacob, 1990), locking (Zweck et al., 2002; Li and Freymueller, 2018), subduction geometries (Christeson et al., 2010) and sediment input (Worthington et al., 2012; Reece et al., 2011) between these two regions suggest major differences in subduction and interface properties within south-central Alaska.

2 Geologic Background and Previous Geophysical Studies of the 1964 Rupture Area

Kodiak Island (*Qikertaq* in Alutiiq) is part of an archipelago that represents an exposed section of the Mesozoic-Tertiary Alaska-Aleutian accretionary complex uplifted either via duplex accretion and underplating (Sample & Fisher, 1986), out-of-sequence splay faulting (e.g., Rowe et al., 2009), or a combination of these processes. The surface exposures consist of Jurassic to Eocene formations bounded by NW-dipping and NE-striking thrusts (Wilson et al., 2015; Fig. 1b). The thrust-bounded units get progressively younger towards the southeast, approaching the current subduction trench offshore (Fig. 1b). Potentially active Quaternary fault systems include the Albatross Bank, Kodiak Shelf and Narrow Cape fault zones (Figs. 1b and 1c). Paleocene granitic intrusions (~58-50 Ma) from ridge subduction (Ayuso et al., 2009; Farris et al., 2006; Fig. 1b) form the mountainous spine of the island interior. In the duplex accretion and underplating scenario for Kodiak Island formation and deformation, a stacked section of marine sediments builds up near the subduction decollement, forming a series of flat-ramp-flat geometries of imbricated material at depth within the overriding plate (Sample & Fisher, 1986; Fig. 1d (i)). The build-up of the underthrust material causes the accretionary prism to grow vertically, with minimal fault penetration or deformation within the overlying sediments. In the splay fault model (Fig. 1d (ii)), the island was uplifted due to deformation on one or several seaward-vergent thrusts possibly rooted at the megathrust.

Prior to our study, the 2007-2008 Multidisciplinary Observations of Onshore Subduction (MOOS; J. Li et al., 2013; Fig. 1a) measured structure and seismicity beneath the Kenai Peninsula in the northern 1964 rupture zone. The MOOS experiment included 34 broadband seismometers deployed at 10-15 km station spacing. Major results include RF imaging showing a 3-5 km-thick low velocity zone (LVZ) sandwiched between the overriding North American plate and the subducting Yakutat microplate (Y. Kim et al., 2014). This low-velocity zone suggests the presence of subducting sediments and/or the presence of fluids within or below the plate interface. Imaging via autocorrelation of P-wave coda from local earthquakes replicates these results and further suggests that S-wave velocity within this zone decreases with depth (D. Kim et al., 2019).

A more recent study of the subducting crust beneath southcentral Alaska suggests that the LVZ extends far beyond the location of the MOOS array. In their scattered-wave imaging of the subduction zone beneath southcentral Alaska, Mann et al. (2022) analyzed seismic data recorded by 218 broadband seismometers across southcentral Alaska. Using data from the Wrangell Volcanism and Lithospheric Fate (WVLF; Fig. 1a) array, the Broadband Experiment Across the Alaska Range (BEAAR; Fig 1a) array, the Transportable Array (TA) and the MOOS array, they found that the LVZ covers > 450 km of the subducting Yakutat terrane (Mann et al., 2022). Our study tests whether these features extend southward, controlling structure beneath northeast Kodiak Island.

3 Data and Methods

3.1 The AACSE

The AACSE took place in 2018-2019 between Kodiak Island and Sanak Island (Abers et al., 2019; Barcheck et al., 2020; Fig. 1a). All experiment data is publicly available and was open

115 immediately upon completion of quality assurance, control and archiving. The AACSE included
116 75 broadband ocean-bottom seismometers (OBS), 30 broadband land seismometers, several
117 dozen additional nearby permanent and EarthScope Transportable Array seismometers,
118 complementary strong motion sensors and absolute- and differential-pressure gauges, and >3,000
119 km of active source wide-angle refraction profiles collected by the R/V *Marcus G Langseth*
120 (Barcheck et al., 2020). The Kodiak node array was deployed in 2019 as a supplement to the
121 larger AACSE. The array consisted of 398 Fairfield autonomous node sensors (from PASSCAL
122 and University of Utah) with 3-component 5-Hz geophones deployed along a ~50 km road
123 network centered on the city of Kodiak (Figs. 1b and 1c). Sensors were deployed at ~200-300 m
124 station spacing over the course of 6 days (May 18-24) and recovered over 3 days (June 19-21).
125 The full nodal array was operational for 25 days (May 25 – June 18). All continuous waveform
126 data from the node array are available in PH5 format via IRIS Data Services (network code 8J
127 from 2019).

128 **3.2 Receiver Function Processing**

129 Previous work shows that the autonomous three-component 5-Hz geophones used in this
130 study can yield high quality RFs comparable with co-located broadband seismometers (Liu et al.,
131 2018; Ward et al., 2018; Ward & Lin, 2017). Like those earlier studies, our short deployment
132 period limited the number of teleseismic events for RF calculation. Out of 52 teleseismic events
133 >Mw 5.0 occurring within the 30°- 90° search radius, we retained 7 events (Table S1; Fig. S1(a)
134 and S1(b)) that met the selection criteria: (1) a magnitude >5.5, (2) a 30° – 90° epicentral
135 distance from the center of the array, and (3) a signal-to-noise ratio (SNR)>3 and an identifiable
136 incident P wave across the array (Figure S1c).

Prior to calculating RFs, we windowed the seismograms from 15 s before to 75 s after the theoretical P arrival. Next, we decimated the waveforms to 50 samples per second using a finite impulse response filter to prevent aliasing. We then removed the mean and the trend and applied a Hanning taper. Finally, we removed the instrument response from the nodal geophones (5 Hz corner frequency). We followed the above steps as outlined by Ward et al. (2018). We then filtered the resulting time series using a bandpass of 0.2 – 2.0 Hz. To groundtruth our waveform processing workflow, we retrieved waveforms for the selected 7 events recorded by AACSE broadband stations deployed within the node array footprint (Z. Li et al., 2020), performed the same pre-processing procedure, and compared the resultant broadband waveforms with the pre-processed nodal time series (Fig. S2).

After preprocessing, we culled additional noisy signals by applying a SNR-based noise reduction procedure which eliminated traces with SNR< 2.0 on the vertical component or SNR < 1.25 on the north component. Then we rotated from the station ZNE (vertical, north, east) coordinate system to the earthquake ZRT (vertical, radial, transverse) system. To compute the RFs for each event, we deconvolved the radial component seismograms with vertical component seismograms at each station using the time-domain iterative deconvolution method (Ligorria & Ammon, 1999) with a Gaussian filter parameter of 2.5 (~1.2 Hz) and 5.0 (~2.4 Hz). All analysis was performed via Python using the open-source rf software package (Eulenfeld, 2020).

Before stacking the RFs, we applied a Ps phase moveout correction using the iasp91 (Kennett & Engdahl, 1991) model and calculated piercing points. We set the piercing point depth at 20 km based on estimates of slab depth (20 – 27 km) beneath the study area from the Slab2.0 model (Hayes et al., 2018), created equal profile boxes along the array (Fig. S3), and then stacked the receiver functions by common conversion points (Fig. 2). Both the stacked 1.2 Hz

and 2.4 Hz RFs were converted to depth (Fig. 2b and 2c) using the rf software and the iasp91 velocity model (Kennett & Engdahl, 1991).

3.3 1-D Synthetic Modeling

To aid our interpretation, we produced synthetic RFs (assuming a ray parameter of 0.05 s/km) that tested three simple velocity-density models of the structure below Kodiak Island. Our primary goal was to evaluate resolution of hypothetical structures near the top of the subducting oceanic crust and compare with previous results from the northern 1964 rupture area. To better account for the RF variability across the Kodiak profile, we selected groups of RFs from three different sections (6-km bins, centered at 10, 22 and 32 km distance along the profile) which showed good signal-to-noise ratios (Fig. 2c) and calculate uncertainties by bootstrap resampling the RFs in each bin before producing the bins' unweighted stacks. We then used the position of the slab Moho Ps arrival on the resultant stacked traces to define the slab Moho depth of the models (Figs. 3a-c).

Model 1 (Table S2; Fig. 3a) is a four-layer model based on the Kim et al. (2014) Kenai Peninsula model beneath the Kenai asperity. The model consists of a featureless upper crust, a 3 km-thick LVZ at the plate interface and an 8 km-thick oceanic crust. To construct model 2 (Table S2; Fig. 3b), we removed the 3-km-thick LVZ from model 1 and calculated synthetics using just the featureless upper crust and the 8 km-thick oceanic crust. For Model 3 (Table S2; Fig. 3c), we eliminated the 3-km LVZ and the top of the oceanic crust resulting in a simple two-layer model with one increase in velocity at the slab Moho depth.

4 Results

4.1 Receiver Function Imaging

Our final common conversion point stack produces a NW-SE-trending, approximately trench-perpendicular profile that samples a ~50 km segment of the Alaska subduction forearc up to 80 km deep (Fig. 2). Both the stacked 1.2 Hz (Fig. 2a) and the stacked 2.4 Hz images (Fig. 2c) show a coherent, SE to NW dipping positive conversion at ~ 30-40 km depth consistent with the expected slab Moho depth from previous studies. For reference, we plotted earthquakes from the AACSE catalog (Ruppert et al., 2021a; Ruppert et al., 2021b) beneath the study area (57.40-58.0 N, 152.083-152.75 W) which are within one standard deviation of the mean hypocentral depth of 24.96 km on our CCP images (black dots in Fig. 2b and 2d). We also plotted the top of the slab depth from Hayes et al. (2018) and inferred the slab Moho depth assuming an 8-km thick oceanic crust (blue and red dashed lines in Fig. 2b and 2d). We do not observe a negative top-of-slab conversion above the positive slab Moho conversion.

We observe intermittent segments of shallow (above ~10 km depth) positive conversions across the length of the profile in our high frequency (2.4 Hz) stacked image (Fig. 2d). One such horizon at ~ 5 km depth extends from about ~8-12 km along the profile, and another beneath Kalsin Bay at ~7 km depth extends from 28-35 km along the profile. Since the depths of these early arrivals vary along the line, the features generating them are likely laterally discontinuous. A mixture of the resultant reverberations and other possible primary arrivals could explain the chaotic character of the traces between ~ 5 km and 35 km depths. Increasing the Gaussian value to 10 (~4.8 Hz) sharpened the amplitudes of coherent arrivals and introduced noise that degraded prominent features such as the slab Moho Ps (Fig. S4(b)).

4.2 Synthetic Modeling Results

Since we were only modeling the features at slab depth and only considering the upgoing Ps conversion, we calculated correlation coefficients of the predicted and the observed

waveforms from 2 s after the P arrival to 10 seconds after the P arrival. Model 1 (Fig. 3a) produced the worst fitting synthetics of all three models (average correlation coefficient of 0.003). Model 2 (Fig. 3b) is a better fit compared to the first model (average correlation coefficient of 0.54). Model 3 (Fig. 3c), the simple two-layer model with an increase in velocity at the slab Moho depth, is the best fitting model with an average correlation coefficient of 0.59. The results suggest that the Vp, Vs and density above the slab Moho must be similar to obtain an optimal fit to the observed data. In other words, introducing additional features in the model above the Moho, even an oceanic crust, creates synthetics that poorly match the observational data.

5 Discussion

5.1 Absence of Oceanic Crust Arrival

In subduction zone environments, RFs are commonly used to investigate plate interface structure since the method exploits the conversion of incident P waves from a teleseismic event to S waves at significant seismic-velocity discontinuities. RFs have identified LVZs along the plate interfaces in subduction zones globally as negative amplitude pulses atop positive amplitude pulses at slab depth (Bostock, 2013; Audet & Kim, 2016). This dipole character has been observed in the Japan (Kawakatsu & Watada, 2007; Akuhara et al., 2017), Cascadia (Janiszewski & Abers, 2015; Ward et al., 2018), Costa Rica (Audet & Schwartz, 2013), Mariana (Tibi et al., 2008), Alaska (Ferris et al., 2003), and the central Mexico (Pérez-Campos et al., 2008; Y. Kim et al., 2012) subduction zones. Depending on how far down dip the study area is located, the negative pulse is typically interpreted as hydrated oceanic crust or mantle hydrated by fluid expelled from the subducting slab due to the low S-wave velocities observed, while the positive amplitude pulse is generally the slab Moho. In Cascadia, Janiszewski and Abers (2015)

228 interpreted the LVZ as metamorphosed sediments, while Bangs et al. (2009) interpreted the LVZ
229 in Nankai as high porosity underthrust sediment. In the northern 1964 segment, Y. Kim et al.
230 (2014) also observed this typical negative-to-positive character, attributing the negative arrivals
231 to an LVZ of subducted marine sediments along the plate interface. Neither our observed nor the
232 preferred synthetic RFs (Figs 2 and 3) feature the negative-positive dipole character observed
233 within the northern 1964 asperity, highlighting a significant difference in RF character within the
234 1964 rupture area. The lack of major arrivals before the positive slab Moho phase suggests three
235 possibilities for subsurface structure: (1) The presence of metasediments at the plate interface
236 with seismic properties similar to the base of the upper plate and top of the subducting slab; (2)
237 there may be a sedimentary layer too thin to be resolved by 1.2 – 2.4 Hz RFs; and (3) there may
238 be no sediments at the plate interface after having been scraped off at the trench during
239 subduction.

240 We note some negative arrivals above the slab Moho at both ends of our profiles (Fig. 2)
241 that may suggest limited areas of low velocity at the interface, perhaps sediments. Plate interface
242 material is commonly inferred from trench sediment input to the subduction zone (Morgan,
243 2004; Underwood, 2007). Approximately 2 km of pelagic and Surveyor Fan sediment (von
244 Huene et al., 2012; Reece et al., 2011; Fig. 1a) comprise the subduction input near Kodiak. It is
245 therefore unlikely that the plate interface beneath Kodiak is devoid of sediments. We suggest that
246 the subduction zone environment has altered the properties of most of the subducted sediment at
247 the interface, thus suppressing the velocity and density contrast between the sediment and the
248 surrounding rock across most of the interface. There is ample evidence from magnetotelluric
249 (Heise et al., 2012), laboratory (Miller et al., 2021) and field studies of exhumed
250 metasedimentary rocks from subduction zone forearcs (Rowe et al., 2009; Rowe et al., 2013)

pointing to instances of hundreds of meters of metamorphosed sediments lining the plate interface. It is likely that the metasedimentary rocks exhumed on Kodiak Island are close enough in seismic properties (e.g., Miller et al., 2021) to the Pacific crust that there is no significant discontinuity at the interface to resolve with Ps RFs. Therefore, the absence of a well-defined LVZ channel at the plate interface beneath our study area does not necessarily mean an absence of subducted sediment. In their study of P- and S-wave velocities of exhumed Kodiak metasediments, Miller et al., (2021) reported anisotropy of ~8-28% in Vp and ~6.5-8% in Vs, with lower wave speeds perpendicular to the rocks' dominant fabric. This suggests an absence of foliation or obliquely foliated rocks conducive for higher wavespeeds beneath our study area.

While the Ps RFs presented here use relatively high frequencies for teleseismic imaging (1.2 – 2.4 Hz), there may be coherent structural layers that are too thin to be resolved. For example, using controlled source seismic reflection data, J. Li et al. (2018) estimated a thin 600-900 m low-velocity channel at shallower (~8-10 km) depths along the plate interface south of Kodiak Island inside the 1938 Mw 8.2 Semidi rupture zone. Our synthetic test of 2.4 Hz Ps RFs showed that although we can detect a 750 m thick LVZ, it is very close to the limit of our resolution (Fig. S4(a)). RFs recovered from a 500 m thick LVZ fall within 2 standard deviations (2σ) of the field data (Fig. S4(a)) suggesting that, if an LVZ exists beneath our study area, it is less than 500 m thick. We also tested using higher frequency observations, 4.8 Hz, but the signal-to-noise ratio of teleseismic sources decreases and the prominent velocity increase interpreted as the slab Moho is only resolved sporadically across the array (Fig. S4(b)). In areas where potential slab Moho arrivals are observed in the 4.8 Hz RF image, we still do not find evidence for an overlying LVZ (Fig. S4(b)). Thus, we cannot rule out a thin LVZ (<500 m) but we can be confident that a thicker LVZ (~3-5 km) like that imaged by Kim et al. (2014) in the Kenai

asperity would be resolvable if it existed beneath our study area. Mann et al. (2022) used scattered P and S coda of teleseismic P waves to successfully image a continuous ~7-km thick low-velocity layer lining the top of the subducted Yakutat crust. While we see reverberations in sections of our profile, their quality is too low to allow for interpretation. The short deployment window (~25 days) and the limited back-azimuth distribution of the events used in this study limits the usefulness of later arrivals.

5.2 Evidence of Rupture Across a Heterogeneous Plate Interface

The simple plate interface structure beneath Kodiak compared to the more complicated plate interface structure beneath the Kenai Peninsula supports other evidence that the 1964 earthquake ruptured multiple segments across distinctive asperities. During the 1964 event, the northern Kenai asperity slipped an average of 18 m, while Kodiak slipped an average of ~10 m (Johnson et al., 1996). Major earthquakes in the Kenai area have a recurrence interval of 700-800 years (Wesson et al., 1999) and the plate interface is strongly locked (Zweck et al., 2002). In Kodiak, the major earthquake recurrence interval is 60 years (Nishenko & Jacob, 1990) and, while the southern end of the Kodiak interface appears strongly locked (S. Li & Freymueller, 2018), locking decreases to the north. Subduction geometry in the Kenai segment is controlled by subduction of the Yakutat microplate, a thick, buoyant oceanic plateau (Christeson et al., 2010) and a thick, subducting sediment package (Y. Kim et al., 2014; Worthington et al., 2012). Beneath Kenai, the plate interface dips shallowly at ~3-4 degrees. In Kodiak, the Pacific plate subducts beneath North America at ~8 degrees, and incoming plate structure includes ~2.5 km-thick sediments from the distal Surveyor Fan (Reece et al., 2011) and the Kodiak-Bowie seamount chain (Fig. 1a).

296 Large megathrust earthquakes at other subduction zones, such as the 1700 M 9.0
297 Cascadia (Wang et al., 2013), 2011 M 9.0 Tohoku-Oki (Wei et al., 2012), 2004 M 9.2 Sumatra
298 (Chlieh et al., 2007), and the 2011 M 8.8 in Chile (Lorito et al., 2011) events encompassed
299 patches of slip rates different from the ambient slip rates within their rupture extents. The
300 ubiquity of heterogeneous coseismic slip during large earthquakes further illustrates that the
301 Great Alaska earthquake entraining multiple major segments during rupture is not unique to the
302 Alaska subduction zone.

303 **5.3 Implications for Rupture Dynamics**

304 Since Ruff (1989) observed that large earthquakes occurred in subduction segments with
305 large sediment inputs, a growing number of studies have linked the occurrence of great
306 megathrust earthquakes with subducted sediment thickness ≥ 1.2 km (e.g., Scholl et al., 2015;
307 Seno, 2017). Many of these studies argue that, depending on the quantity and mineralogical
308 properties of the subducted sediments, a sedimentary layer can level inter-plate relief facilitating
309 rupture propagation over long distances (Ruff, 1989). Numerical modeling (e.g., Brizzi et al.,
310 2020) suggests that a total absence of sediments at the plate interface would yield significantly
311 smaller earthquakes (M<8.5) compared to interfaces with just a 1.5 km thick sediment layer. The
312 2011 M 9 Tohoku-Oki provides an example of a great earthquake that occurred with < 1 km
313 thick sediment layer at the interface (Heuret et al., 2012). We did not find any recorded great
314 megathrust earthquakes occurring at subduction zones with no trench sediment input.

315 In their study of Kodiak region seismicity between 1964 and 2001, Doser et al. (2002)
316 found that, while most earthquakes occur within the downgoing plate, several events beneath
317 southern Kodiak Island have depths and thrust faulting mechanisms consistent with seismicity on
318 the interface, suggesting the existence of subducted topographic features such as seamounts from

the Kodiak-Bowie chain (Fig. 1a) beneath Kodiak that have not been smoothed with a thick sediment padding. Detailed seismicity studies on the Kenai Peninsula using the MOOS array show a well-defined seismic zone concentrated in the down-going plate, just below the plate boundary, that parallels the megathrust zone and is dominated by normal faulting mechanisms (J. Li et al., 2013). In contrast to observations in the Kodiak region, active thrusting and seismicity on the plate interface itself was absent (J. Li et al., 2013), possibly related to thick sediment subduction between the North American and Yakutat plates smoothening localized asperities and favoring uniform rupture in great earthquakes but not small heterogenous ruptures.

6 Conclusions

We analyzed teleseismic P waves from 398 autonomous three-component 5-Hz nodal geophones on Kodiak Island as part of the Alaska Amphibious Community Seismic Experiment. We calculated RFs with a Gaussian value of 2.5 (~1.2 Hz) and a Gaussian value of 5.0 (~2.4 Hz). The lower frequency (1.2 Hz) RFs were comparable to RFs from near-collocated broadband seismometers, and the higher frequency (2.4 Hz) RFs image produced more details. In both low and high frequency images, there is a coherent, SE to NW dipping positive phase at the expected slab Moho depth but no observable negative arrival to indicate phase conversions at the oceanic crust. To help explain the observed RFs, we calculated synthetic RFs from 1-D models. These synthetic tests suggest that the overriding forearc material and Pacific oceanic crust have nearly identical seismic velocities and densities. We conclude that the 1964 Great Alaska Earthquake ruptured beyond the extent of the low-velocity shear zone observed in the Kenai asperity into a structural setting beneath Kodiak Island with little seismic contrast across the plate boundary interface.

Data and Resources:

The nodal seismic data used in this study are available from the IRIS DMC (dmc.iris.edu) under the network code 8J (doi: 10.7914/SN/8J_2019). The IRIS DMC is supported by the National Science Foundation under Cooperative Support Agreement EAR-1851048. We obtained digital elevation data for Figures 1a and 1c from the GEBCO Compilation Group (doi:10.5285/a29c5465-b138-234d-e053-6c86abc040b9, last accessed August 2021). Geologic map data for Figure 1b and 1c was obtained from the USGS Scientific Investigations map 3340 (https://pubs.er.usgs.gov/publication/sim3340, last accessed August 2021).

Acknowledgements:

We acknowledge that the Alaska Amphibious Community Seismic Experiment was conducted within the present, ancestral, and unceded lands and waters of the Alutiiq/Sugpiaq, Unangax, Aleut and Central Yup'ik peoples. Seismic stations on Kodiak Island (Qikertaq) were placed within lands of the Koniag Alaska Native Regional Corporation, specifically within the lands of Ahkiok, Anton Larsen Bay, Larsen Bay, Leisnoi, Old Harbor, and Ouzinkie Alaska Native Village Corporations and Sun'aq (Kodiak City). We are grateful to these communities and cultures for the opportunity to learn about their lands and waters.

The Alaska Amphibious Community Seismic Experiment (AACSE) was funded by the NSF award OCE-1654568 to Cornell University. Nodal geophones were provided by the Incorporated Research Institutions for Seismology-Portable Array Seismic Studies of the Continental Lithosphere (IRIS-PASSCAL) Instrument Center, which is supported by the National Science Foundation's Seismological Facilities for the Advancement of Geoscience (SAGE) Award under Cooperative Support Agreement EAR-1851048. Dr. Jamie Farrell (University of Utah) provided additional nodes and assisted with logistics. This research was partially supported by EAR-1950328. The authors would also like to acknowledge Lucia

Gonzales (University of Texas at El Paso), Dr. Jenny Nakai (USGS - Alaska Volcano Observatory), and Dr. Doug Wiens (Washington University in St. Louis), for their work on the node deployment. Dr. Aubreya Adams (Colgate University), Alyssa Fintel (Purdue University) and other summer undergraduate participants assisted with node retrieval and demobilization. The authors are also grateful to Dr. Daoyuan Sun, Dr. Patricia Persaud, and an anonymous reviewer for their helpful comments that improved this article.

References

Abers, G. A., Adams, A. N., Haeussler, P. J., Roland, E., Shore, P. J., Schwartz, S. Y., Sheehan, A. F., Shillington, D. J., Webb, S., Wiens, D. A., and Worthington, L. L. (2019). AACSE: The Alaska amphibious community seismic experiment. *EOS Trans. AGU*, Online publ. 26 March 2019. https://eos.org/project-updates/examining-alaskas-earthquakes-on-land-and-sea.

Akuhara, T., Mochizuki, K., Kawakatsu, H., & Takeuchi, N. (2017). A fluid-rich layer along the Nankai trough megathrust fault off the Kii Peninsula inferred from receiver function inversion. *J Geophys Res B Solid Earth Planets*, *122*(8), 6524–6537. https://doi.org/10.1002/2017JB013965

Audet, P., & Kim, Y. (2016). Teleseismic constraints on the geological environments of deep episodic slow earthquakes in subduction zone forearcs: A review. *Tectonophysics*, *670*, 1-15. https://doi.org/10.1016/j.tecto.2016.01.005

Audet, P., & Schwartz, S. Y. (2013). Hydrologic control of forearc strength and seismicity in the Costa Rican subduction zone. *Nat Geosci*, *6(10)*, 852-855. https://doi.org/10.1038/ngeo1927

Ayuso, R. A., Haeussler, P. J., Bradley, D. C., Farris, D. W., Foley, N. K., & Wandless, G. A.

(2009). The role of ridge subduction in determining the geochemistry and Nd–Sr–Pb isotopic evolution of the Kodiak batholith in southern Alaska. *Tectonophysics*, *464*(1–4), 137–163. https://doi.org/10.1016/j.tecto.2008.09.029

Bangs, N. L. B., Moore, G. F., Gulick, S. P. S., Pangborn, E. M., Tobin, H. J., Kuramoto, S., & Taira, A. (2009). Broad, weak regions of the Nankai Megathrust and implications for shallow coseismic slip. *Earth Planet Sci Lett*, *284*(1–2), 44–49. https://doi.org/10.1016/j.epsl.2009.04.026

Barcheck, G., Abers, G. A., Adams, A. N., Bécel, A., Collins, J., Gaherty, J. B., Haeussler, P.J., Li, Z., Moore, G., Onyango, E. A., Roland, E., Sampson, D. E., Schwartz, S. Y., Sheehan, A. F., Shillington, D. J., Shore, P. J., Webb, S., Wiens, D. A., & Worthington, L. L. (2020). The Alaska Amphibious Community Seismic Experiment. *Seismol Res Lett*, *91*(6), 3054–3063. https://doi.org/10.1785/0220200189

Bostock, M. G. (2013). The Moho in subduction zones. *Tectonophysics*, *609*, 547–557. https://doi.org/10.1016/j.tecto.2012.07.007

Brizzi, S., Zelst, I., Funiciello, F., Corbi, F., & Dinther, Y. (2020). How Sediment Thickness Influences Subduction Dynamics and Seismicity. *J Geophys Res B Solid Earth Planets*, *125*(8), e2019JB018964. https://doi.org/10.1029/2019JB018964

Chlieh, M., Avouac, J. P., Hjorleifsdottir, V., Song, T. R. A., Ji, C., Sieh, K., Sladen, A., Hebert, H., Prawirodirdjo, L., Bock, L., & Galetzka, J. (2007). Coseismic Slip and Afterslip of the Great Mw 9.15 Sumatra-Andaman Earthquake of 2004. *Bull Seismol Soc Am*, *97*(1A), S152–S173. https://doi.org/10.1785/0120050631

Christensen, D. H., & Beck, S. L. (1994). The rupture process and tectonic implications of the great 1964 Prince William Sound earthquake. *Pure Appl Geophys*, *142*(1), 29–53.

Christeson, G. L., Gulick, S. P. S., van Avendonk, H. J. A., Worthington, L. L., Reece, R. S., & Pavlis, T. L. (2010). The Yakutat terrane: Dramatic change in crustal thickness across the Transition fault, Alaska. *Geology*, *38*(10), 895–898. https://doi.org/10.1130/G31170.1

Connelly, W. (1978). Uyak Complex, Kodiak Islands, Alaska: A Cretaceous subduction complex. *Geol Soc Am Bull*, *89*(5), 755. https://doi.org/10.1130/0016-7606(1978)89<755:UCKIAA>2.0.CO;2

Doser, D. I., Brown, W. A., & Velasquez, M. (2002). Seismicity of the Kodiak Island Region (1964-2001) and Its Relation to the 1964 Great Alaska Earthquake. *Bull Seismol Soc Am*, *92*(8), 3269–3292. https://doi.org/10.1785/0120010280

Eulenfeld, T. (2020). rf: Receiver function calculation in seismology. *Journal of Open Source Software*, *5*(48), 1808. https://doi.org/10.21105/joss.01808

Farris, D. W., Haeussler, P., Friedman, R., Paterson, S. R., Saltus, R. W., & Ayuso, R. (2006). Emplacement of the Kodiak batholith and slab-window migration. *Geol Soc Am Bull*, *118*(11–12), 1360–1376. https://doi.org/10.1130/B25718.1

Ferris, A., Abers, G. A., Christensen, D. H., & Veenstra, E. (2003). High resolution image of the subducted Pacific (?) plate beneath central Alaska, 50–150 km depth. *Earth Planet Science Lett*, *214*(3–4), 575–588. https://doi.org/10.1016/S0012-821X(03)00403-5

Hayes, G. P., Moore, G. L., Portner, D. E., Hearne, M., Flamme, H., Furtney, M., & Smoczyk, G. M. (2018). Slab2, a comprehensive subduction zone geometry model. *Science*, *362*(6410), 58–61. https://doi.org/10.1126/science.aat4723

Heise, W., Caldwell, T. G., Hill, G. J., Bennie, S. L., Wallin, E., & Bertrand, E. A. (2012). Magnetotelluric imaging of fluid processes at the subduction interface of the Hikurangi margin, New Zealand. *Geophys Res Lett*, *39*(4). https://doi.org/10.1029/2011GL050150

Heuret, A., Conrad, C. P., Funiciello, F., Lallemand, S., & Sandri, L. (2012). Relation between subduction megathrust earthquakes, trench sediment thickness and upper plate strain. *Geophys Res Lett*, *39*(5). https://doi.org/10.1029/2011GL050712

von Huene, R., Miller, J. J., & Weinrebe, W. (2012). Subducting plate geology in three great earthquake ruptures of the western Alaska margin, Kodiak to Unimak. *Geosphere*, *8*(3), 628–644. https://doi.org/10.1130/GES00715.1

Ichinose, G., Somerville, P., Thio, H. K., Graves, R., & O'Connell, D. (2007). Rupture process of the 1964 Prince William Sound, Alaska, earthquake from the combined inversion of seismic, tsunami, and geodetic data. *J Geophys Res*, *112*(B7), B07306. https://doi.org/10.1029/2006JB004728

Janiszewski, H. A., & Abers, G. A. (2015). Imaging the Plate Interface in the Cascadia Seismogenic Zone: New Constraints from Offshore Receiver Functions. *Seismol Res Lett*, *86*(5), 1261–1269. https://doi.org/10.1785/0220150104

Johnson, J. M., Satake, K., Holdahl, S. R., & Sauber, J. (1996). The 1964 Prince William Sound earthquake: Joint inversion of tsunami and geodetic data. *J Geophys Res B Solid Earth Planets*, *101*(B1), 523–532. https://doi.org/10.1029/95JB02806

Kanamori, H. (1977). The energy release in great earthquakes. *J Geophys Res*, *82*(20), 2981–2987. https://doi.org/10.1029/JB082i020p02981

Kawakatsu, H., & Watada, S. (2007). Seismic Evidence for Deep-Water Transportation in the Mantle. *Science*, *316*(5830), 1468–1471. https://doi.org/10.1126/science.1140855

Kennett, B. L. N., & Engdahl, E. R. (1991). Traveltimes for global earthquake location and phase identification. *Geophys J Int*, *105*(2), 429–465. https://doi.org/10.1111/j.1365-246X.1991.tb06724.x

Kim, D., Keranen, K. M., Abers, G. A., & Brown, L. D. (2019). Enhanced Resolution of the Subducting Plate Interface in Central Alaska From Autocorrelation of Local Earthquake Coda. *J Geophys Res B Solid Earth Planets*, *124*(2), 1583–1600. https://doi.org/10.1029/2018JB016167

Kim, Y., Miller, M. S., Pearce, F., & Clayton, R. W. (2012). Seismic imaging of the Cocos plate subduction zone system in central Mexico. *G-cubed*, *13*(7). https://doi.org/10.1029/2012GC004033

Kim, Y., Abers, G. A., Li, J., Christensen, D., Calkins, J., & Rondenay, S. (2014). Alaska Megathrust 2: Imaging the megathrust zone and Yakutat/Pacific plate interface in the Alaska subduction zone. *J Geophys Res B Solid Earth Planets*, *119*(3), 1924–1941. https://doi.org/10.1002/2013JB010581

Li, J., Abers, G. A., Kim, Y., & Christensen, D. (2013). Alaska megathrust 1: Seismicity 43 years after the great 1964 Alaska megathrust earthquake. *J Geophys Res B Solid Earth Planets*, *118*(9), 4861–4871. https://doi.org/10.1002/jgrb.50358

Li, J., Shillington, D. J., Saffer, D. M., Bécel, A., Nedimović, M. R., Kuehn, H., Webb, S. C., Keranen, K. M., & Abers, G. A. (2018). Connections between subducted sediment, pore-fluid pressure, and earthquake behavior along the Alaska megathrust. *Geology*, *46*(4), 299–302. https://doi.org/10.1130/G39557.1

Li, S., & Freymueller, J. T. (2018). Spatial Variation of Slip Behavior Beneath the Alaska Peninsula Along Alaska-Aleutian Subduction Zone. *Geophys Res Lett*, *45*(8), 3453–3460. https://doi.org/10.1002/2017GL076761

Li, Z., Wiens, D., & Shen, W. (2020). Crust and Uppermost Mantle Structure of the Alaska Subduction Zone from Joint Inversion of Rayleigh Wave Dispersion and Receiver

480 Functions. *The 2020 AGU Fall Meeting,* Online, 1-17 December, Abstract T055-04.
481 Ligorria, J. P., & Ammon, C. J. (1999). Iterative Deconvolution and Receiver-Function
482 Estimation. *Bull Seismol Soc Am*, *89*(5), 1395–1400.
483 Liu, G., Persaud, P., & Clayton, R. W. (2018). Structure of the Northern Los Angeles Basins
484 Revealed in Teleseismic Receiver Functions from Short-Term Nodal Seismic Arrays.
485 *Seismol Res Lett*, *89*(5), 1680–1689. https://doi.org/10.1785/0220180071
486 Lorito, S., Romano, F., Atzori, S., Tong, X., Avallone, A., McCloskey, J., Cocco, M., Boschi, E.,
487 & Piatanesi, A. (2011). Limited overlap between the seismic gap and coseismic slip of the
488 great 2010 Chile earthquake. *Nat Geosci*, *4*(3), 173–177. https://doi.org/10.1038/ngeo1073
489 Mann, M. E., Abers, G. A., Daly, K. A., & Christensen, D. H. (2022). Subduction of an Oceanic
490 Plateau Across Southcentral Alaska: Scattered-Wave Imaging. *J Geophysl Res B Solid*
491 *Earth Planets*, *127*(1), e2021JB022697. https://doi.org/10.1029/2021JB022697
492 Miller, P. K., Saffer, D. M., Abers, G. A., Shillington, D. J., Bécel, A., Li, J., & Bate, C. (2021).
493 P- and S-Wave Velocities of Exhumed Metasediments From the Alaskan Subduction Zone:
494 Implications for the In Situ Conditions Along the Megathrust. *Geophys Res Lett*, *48*(20),
495 e2021GL094511. https://doi.org/10.1029/2021GL094511
496 Morgan, J. K. (2004). Consolidation state and strength of underthrust sediments and evolution of
497 the décollement at the Nankai accretionary margin: Results of uniaxial reconsolidation
498 experiments. *J Geophys Res*, *109*(B3), B03102. https://doi.org/10.1029/2002JB002335
499 Nishenko, S. P., & Jacob, K. H. (1990). Seismic potential of the Queen Charlotte-Alaska-
500 Aleutian Seismic Zone. *J Geophys Res*, *95*(B3), 2511.
501 https://doi.org/10.1029/JB095iB03p02511
502 Paterson, S. R., & Sample, J. C. (1988). The development of folds and cleavages in slate belts by

underplating in accretionary complexes: A comparison of the Kodiak Formation, Alaska and the Calaveras Complex, California. *Tectonics*, *7*(4), 859–874. https://doi.org/10.1029/TC007i004p00859

Pérez-Campos, X., Kim, Y., Husker, A., Davis, P. M., Clayton, R. W., Iglesias, A., Pacheco, J. F., Singh, S. K., Manea, V. C., & Gurnis, M. (2008). Horizontal subduction and truncation of the Cocos Plate beneath central Mexico. *Geophys Res Lett*, *35*(18), L18303. https://doi.org/10.1029/2008GL035127

Reece, R. S., Gulick, S. P. S., Horton, B. K., Christeson, G. L., & Worthington, L. L. (2011). Tectonic and climatic influence on the evolution of the Surveyor Fan and Channel system, Gulf of Alaska. *Geosphere*, *7*(4), 830–844. https://doi.org/10.1130/GES00654.1

Rowe, Christen D, Meneghini, F., & Moore, J. C. (2009). Fluid-rich damage zone of an ancient out-of-sequence thrust, Kodiak Islands, Alaska. *Tectonics*, *28*(1). https://doi.org/10.1029/2007TC002126

Rowe, Christie D, Moore, J. C., & Remitti, F. (2013). The thickness of subduction plate boundary faults from the seafloor into the seismogenic zone. *Geology*, *41*(9), 991–994. https://doi.org/10.1130/G34556.1

Ruff, L. J. (1989). Do Trench Sediments Affect Great Earthquake Occurrence in Subduction Zones? In *Subduction Zones Part II* (pp. 263–282). Basel: Birkhäuser Basel. https://doi.org/10.1007/978-3-0348-9140-0_9

Ruppert, N. A., Barcheck, G., & Abers, G. A. (2021a). AACSE earthquake catalog: May-December, 2018. http://hdl.handle.net/11122/11418

Ruppert, N. A., Barcheck, G., & Abers, G. A. (2021b). AACSE earthquake catalog: January-August, 2019. http://hdl.handle.net/11122/11967

526 Sample, J. C., & Fisher, D. M. (1986). Duplex accretion and underplating in an ancient
527 accretionary complex, Kodiak Islands, Alaska. *Geology*, *14*(2), 160–163.
528 https://doi.org/10.1130/0091-7613(1986)14<160:DAAUIA>2.0.CO;2
529 Scholl, D. W., Kirby, S. H., von Huene, R., Ryan, H., Wells, R. E., & Geist, E. L. (2015). Great
530 (≥Mw8.0) megathrust earthquakes and the subduction of excess sediment and
531 bathymetrically smooth seafloor. *Geosphere*, *11*(2), 236–265.
532 https://doi.org/10.1130/GES01079.1
533 Seno, T. (2017). Subducted sediment thickness and M w 9 earthquakes. *J Geophysl Res B Solid*
534 *Earth Planet*, *122*(1), 470–491. https://doi.org/10.1002/2016JB013048
535 Suito, H., & Freymueller, J. T. (2009). A viscoelastic and afterslip postseismic deformation
536 model for the 1964 Alaska earthquake. *J Geophys Res B Solid Earth Planets*, *114*(B11).
537 https://doi.org/10.1029/2008JB005954
538 Tibi, R., Wiens, D. A., & Yuan, X. (2008). Seismic evidence for widespread serpentinized
539 forearc mantle along the Mariana convergence margin. *Geophys Res Lett*, *35*(13), L13303.
540 https://doi.org/10.1029/2008GL034163
541 Tsuji, T., Ashi, J., & Ikeda, Y. (2014). Strike-slip motion of a mega-splay fault system in the
542 Nankai oblique subduction zone. *Earth Planets Space*, *66*(1), 120.
543 https://doi.org/10.1186/1880-5981-66-120
544 Underwood, M. B. (2007). Sediment Inputs to Subduction Zones: Why lithostratigraphy and clay
545 mineralogy matter. In *The Seismogenic Zone of Subduction Thrust Faults* (pp. 42–85).
546 Columbia University Press. https://doi.org/10.7312/dixo13866-003
547 Wang, P. L., Engelhart, S. E., Wang, K., Hawkes, A. D., Horton, B. P., Nelson, A. R., & Witter,
548 R. C. (2013). Heterogeneous rupture in the great Cascadia earthquake of 1700 inferred from

549 coastal subsidence estimates. *J Geophys Res B Solid Earth Planets*, *118*(5), 2460–2473.
550 https://doi.org/10.1002/jgrb.50101
551 Ward, K. M., & Lin, F. (2017). On the Viability of Using Autonomous Three-Component Nodal
552 Geophones to Calculate Teleseismic Ps Receiver Functions with an Application to Old
553 Faithful, Yellowstone. *Seismol Res Lett*, *88*(5), 1268–1278.
554 https://doi.org/10.1785/0220170051
555 Ward, K. M., Lin, F., & Schmandt, B. (2018). High-Resolution Receiver Function Imaging
556 Across the Cascadia Subduction Zone Using a Dense Nodal Array. *Geophys Res Lett*,
557 *45*(22), 12,218-12,225. https://doi.org/10.1029/2018GL079903
558 Wei, S., Graves, R., Helmberger, D., Avouac, J. P., & Jiang, J. (2012). Sources of shaking and
559 flooding during the Tohoku-Oki earthquake: A mixture of rupture styles. *Earth Planet Sci*
560 *Lett*, *333–334*, 91–100. https://doi.org/10.1016/j.epsl.2012.04.006
561 Wesson, R. L., Frankel, A. D., Mueller, C. S., & Harmsen, S. C. (1999). Probabilistic seismic
562 hazard maps of Alaska. *US Geol. Surv. Open-File Rept. 99-36*.
563 https://doi.org/10.3133/ofr9936
564 Wilson, F. H., Hults, C. P., Mull, C. G., & Karl, S. M. (2015). *Geologic map of Alaska*. *Scientific*
565 *Investigations Map*. *US Geol. Surv. Open-File Rept. 3340*. https://doi.org/10.3133/sim3340
566 Worthington, L. L., Van Avendonk, H. J. A., Gulick, S. P. S., Christeson, G. L., & Pavlis, T. L.
567 (2012). Crustal structure of the Yakutat terrane and the evolution of subduction and
568 collision in southern Alaska. *J Geophys Res B Solid Earth Planets*, *117*(B1).
569 https://doi.org/10.1029/2011JB008493
570 Zweck, C., Freymueller, J. T., & Cohen, S. C. (2002). Three-dimensional elastic dislocation
571 modeling of the postseismic response to the 1964 Alaska earthquake. *J Geophys Res B Solid*

572 *Earth Planets*, *107*(B4), ECV-1. https://doi.org/10.1029/2001JB000409

573

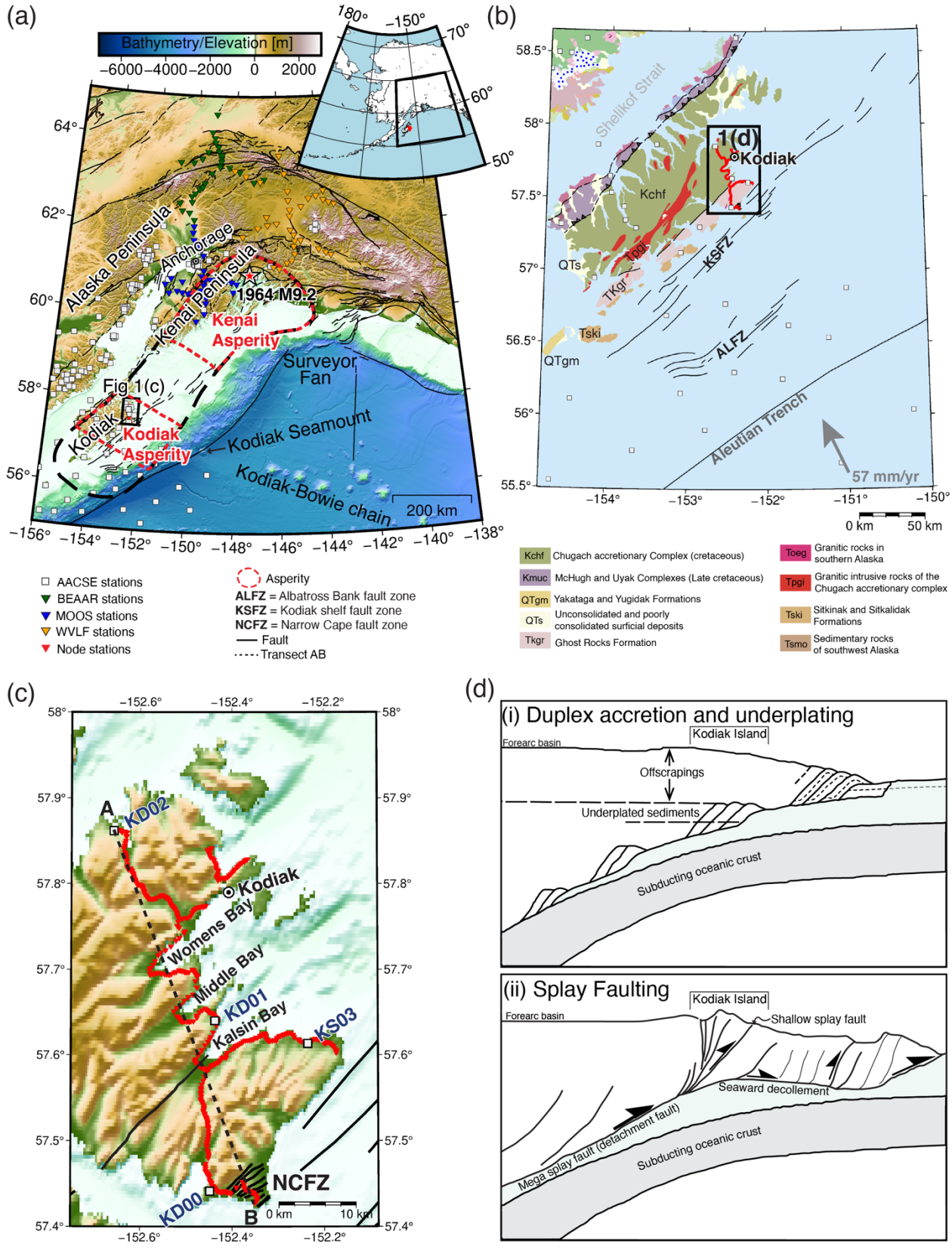
(a)
Bathymetry/Elevation [m]
−6000 −4000 −2000 0 2000
Alaska Peninsula
Anchorage
Kenai Peninsula
1964 M9.2
Kenai Asperity
Surveyor Fan
Fig 1(c)
Kodiak
Kodiak Asperity
Kodiak Seamount
Kodiak-Bowie chain
200 km
AACSE stations
BEAAR stations
MOOS stations
WVLF stations
Node stations
Asperity
ALFZ = Albatross Bank fault zone
KSFZ = Kodiak shelf fault zone
NCFZ = Narrow Cape fault zone
Fault
Transect AB
(b)
Shellikof Strait
1(d)
Kodiak
Kchf
QTs
Tpgi
TKgr
KSFZ
Tski
QTgm
ALFZ
Aleutian Trench
57 mm/yr
0 km 50 km
Kchf Chugach accretionary Complex (cretaceous)
Kmuc McHugh and Uyak Complexes (Late cretaceous)
QTgm Yakataga and Yugidak Formations
QTs Unconsolidated and poorly consolidated surficial deposits
Tkgr Ghost Rocks Formation
Toeg Granitic rocks in southern Alaska
Tpgi Granitic intrusive rocks of the Chugach accretionary complex
Tski Sitkinak and Sitkalidak Formations
Tsmo Sedimentary rocks of southwest Alaska
(c)
A
KD02
Kodiak
Womens Bay
Middle Bay
KD01
Kalsin Bay
KS03
NCFZ
KD00
B
0 km 10 km
(d)
(i) Duplex accretion and underplating
Forearc basin
Kodiak Island
Offscrapings
Underplated sediments
Subducting oceanic crust
(ii) Splay Faulting
Forearc basin
Kodiak Island
Shallow splay fault
Seaward decollement
Mega splay fault (detachment fault)
Subducting oceanic crust

Figure 1. (a) Shaded topographic map and faults of southern Alaska and the Kodiak Islands region. MOOS array (blue triangles), BEAAR array (green triangles), WVLF array (Orange triangles). **(b)** Geology map of the Kodiak Islands region. Refer to Wilson et al., (2015) for geologic unit explanation. **(c)** Shaded topographic map of the study area. **(d)** Schematic diagrams depicting scenarios for Kodiak Island formation and deformation. (i) Modified from Paterson and Sample (1988) illustrates the duplex accretion and underplating scenario. (ii) Modified from Tsuji et al., (2014) illustrates the splay faulting scenario.

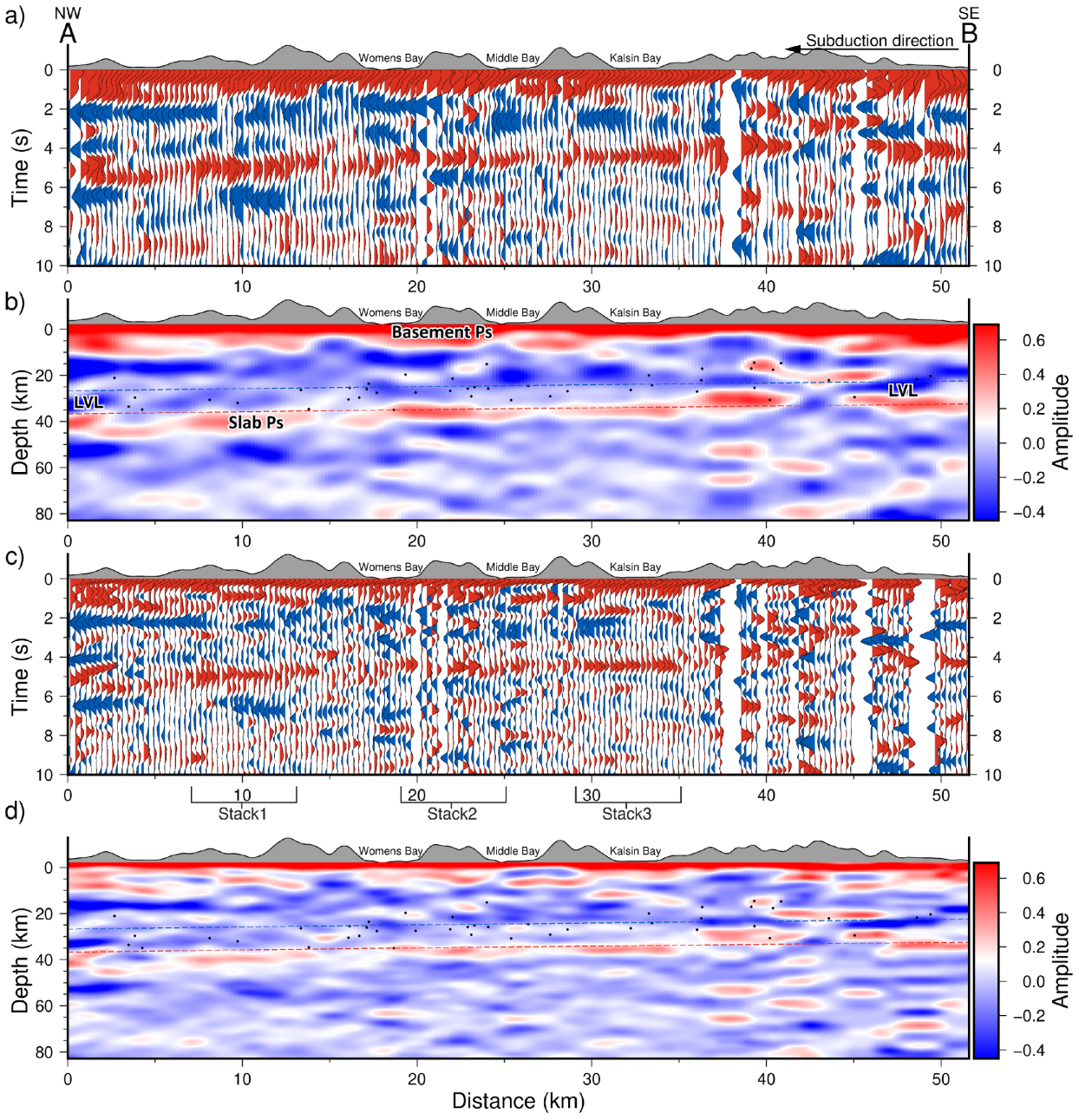

583

584 **Figure 2. (a)** Stacked radial receiver functions with a Gaussian value of 2.5 (~ 1.2 Hz). **(b)** ~1.2

585 Hz CCP image for transect A-B. Note the clear lack of a low velocity channel at the plate

586 interface (Red = Positive, Blue = Negative). For reference, earthquakes from the AACSE catalog

587 (black dots) and the top-of-slab depth from Hayes et al. (2018) is plotted as blue dashes and

588 inferred Moho surface assuming an 8-km thick oceanic crust is plotted as red dashes. Vertical

589 exaggeration = 0.135. **(c)** Stacked radial receiver functions with a Gaussian value of 5.0 (~2.4
590 Hz). Stack1, Stack2 and Stack3 show the locations of the receiver functions stacked and plotted
591 in Figure 3 to compare with synthetics. **(d)** ~2.4 Hz CCP image for transect A-B. Note the clear
592 lack of a low velocity channel at the plate interface.

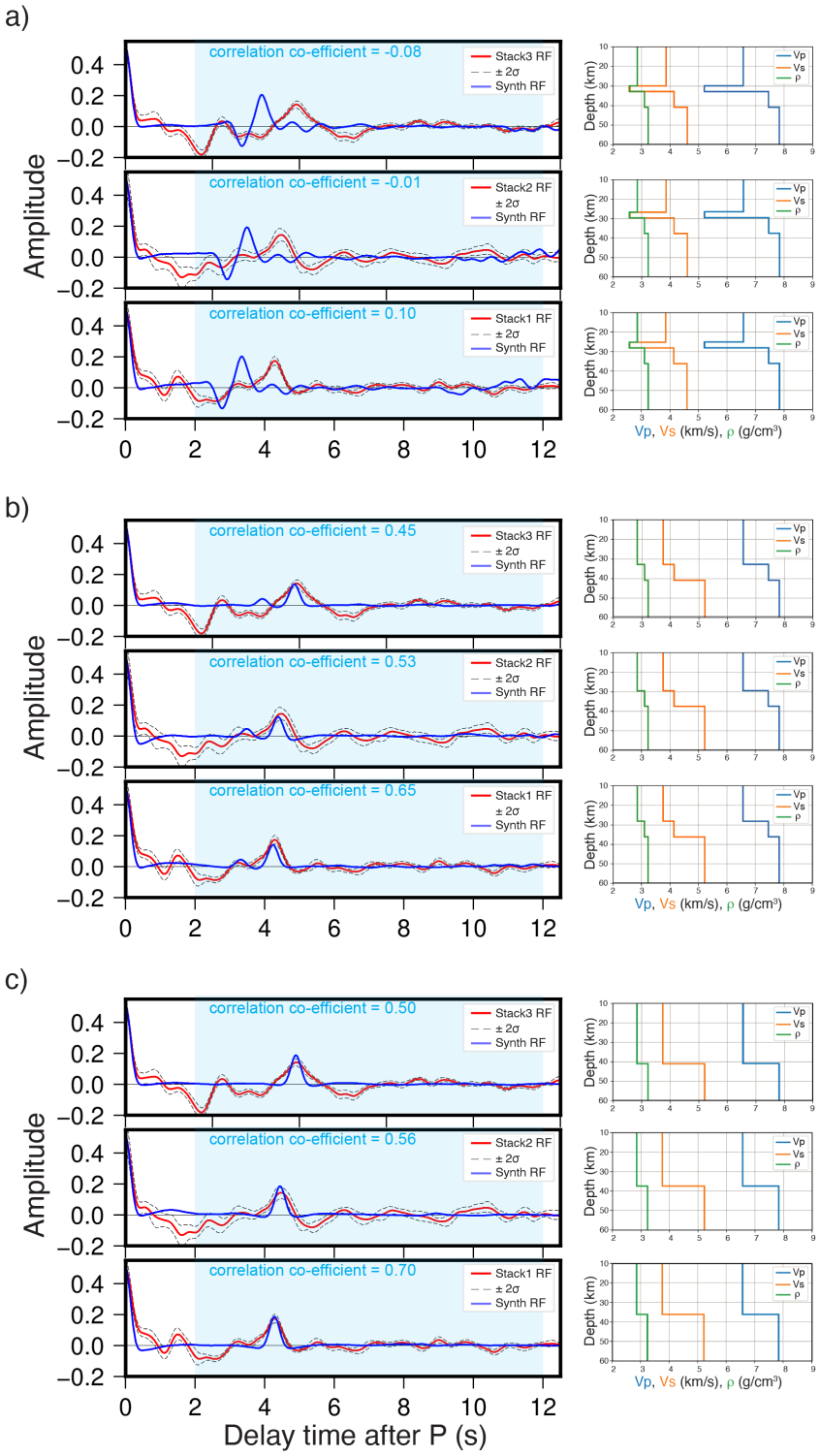

Figure 3. Each set of 3 plots represents synthetic modeling results (black dashed lines) overlaid on stacked field RFs (red lines) centered at 10 km (top), 22 km (middle) and 3 km (bottom), field RF uncertainties are plotted as black dashed lines. The right column contains the velocity models

used to calculate the synthetic RFs on the left. **(a)** Model 1 is analogous to the Kenai observations by Y. Kim et al., (2014). **(b)** Model 2 has no LVZ above the subduction slab. **(c)** Model 3 is the best-fitting model, it only contains the slab Moho.

Geophysical Research Letters

Supporting Information for

Subduction Zone Interface Structure within the Southern M_w9.2 1964 Great Alaska Earthquake Asperity: Constraints from Receiver Functions Across a Spatially Dense Node Array

Evans A. Onyango[1]*, Lindsay L. Worthington[1], Brandon Schmandt[1], Geoffrey Abers[2]

[1]Department of Earth and Planetary Sciences, Northrop Hall, 221 Yale Blvd NE, University of New Mexico, Albuquerque, New Mexico 87131, USA.

[2]Department of Earth and Atmospheric Sciences, Cornell University, 112 Hollister Drive, Ithaca, NY, 14853-1504, USA.

Contents of this file

Introduction

This supporting file contains the following figures and table:

Figure S1: Back azimuthal distribution, locations and example of teleseismic earthquakes used for receiver function analysis.
Figure S2: Comparison of near co-located nodal and broadband station waveforms and receiver functions.
Figure S3: Map view of piercing points at 20 km depth.
Figure S4: Simple synthetic test of different LVZ thicknesses, and profile of receiver functions with a Gaussian value of 10 (~4.8 Hz).
Table S1: Teleseismic events selected for this study.
Table S2: One-Dimensional model parameters.

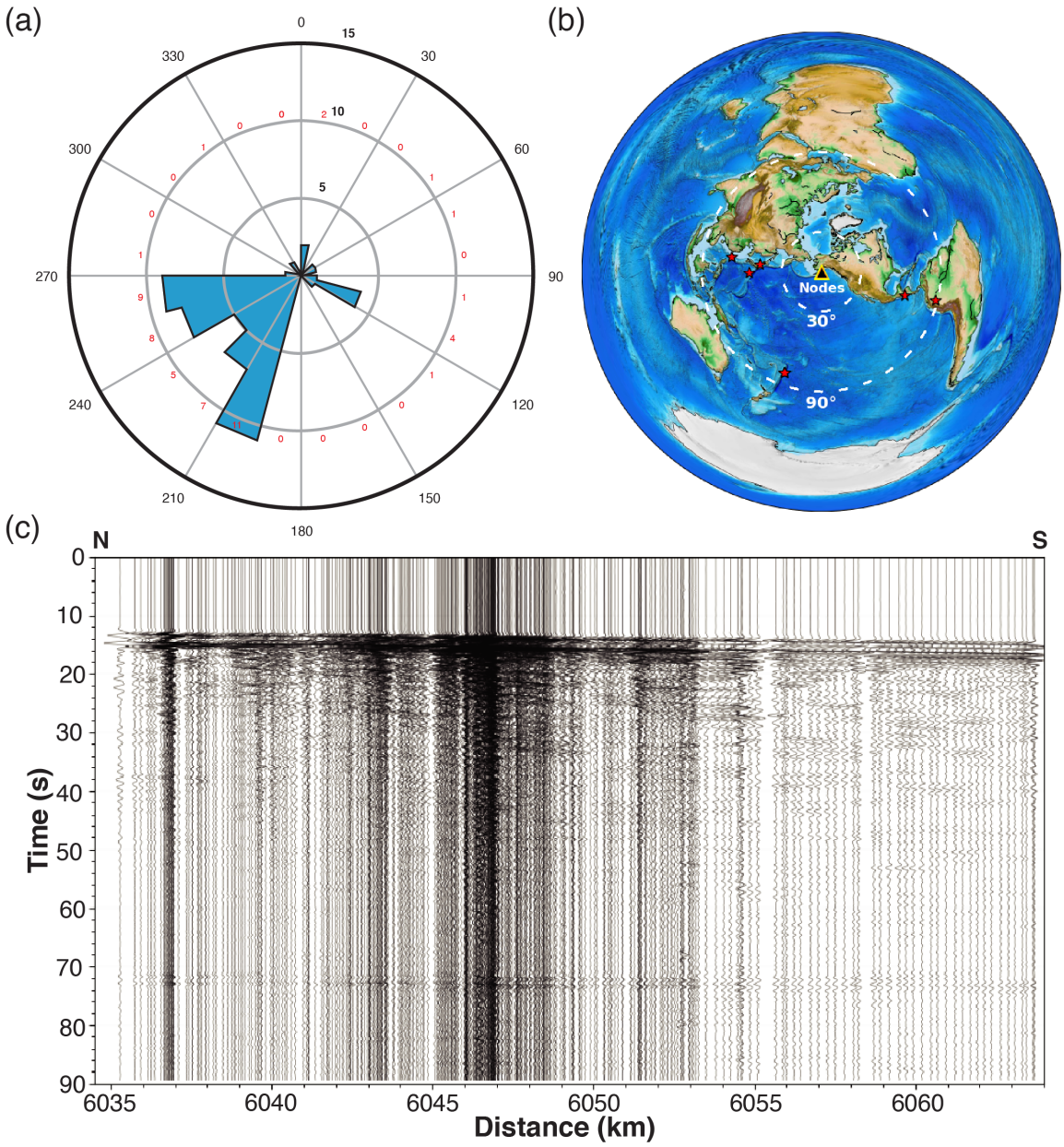

Figure S1. (a) Back azimuthal distribution of teleseismic events >5.0 MW within the 30° – 90° distance window, occurring between May 23, 2019, and June 17, 2019. **(b)** Location of the 7 events selected for receiver function calculation. **(c)** Record section plot of one of the events used for receiver function calculation after instrument response removal, and a bandpass filter (0.2-2 Hz). Amplitudes normalized with

each trace. This Mw 6.3 occurred on 04 June 2019, 04:39:17 UTC at ~430 km depth southeast of Honshu, Japan.

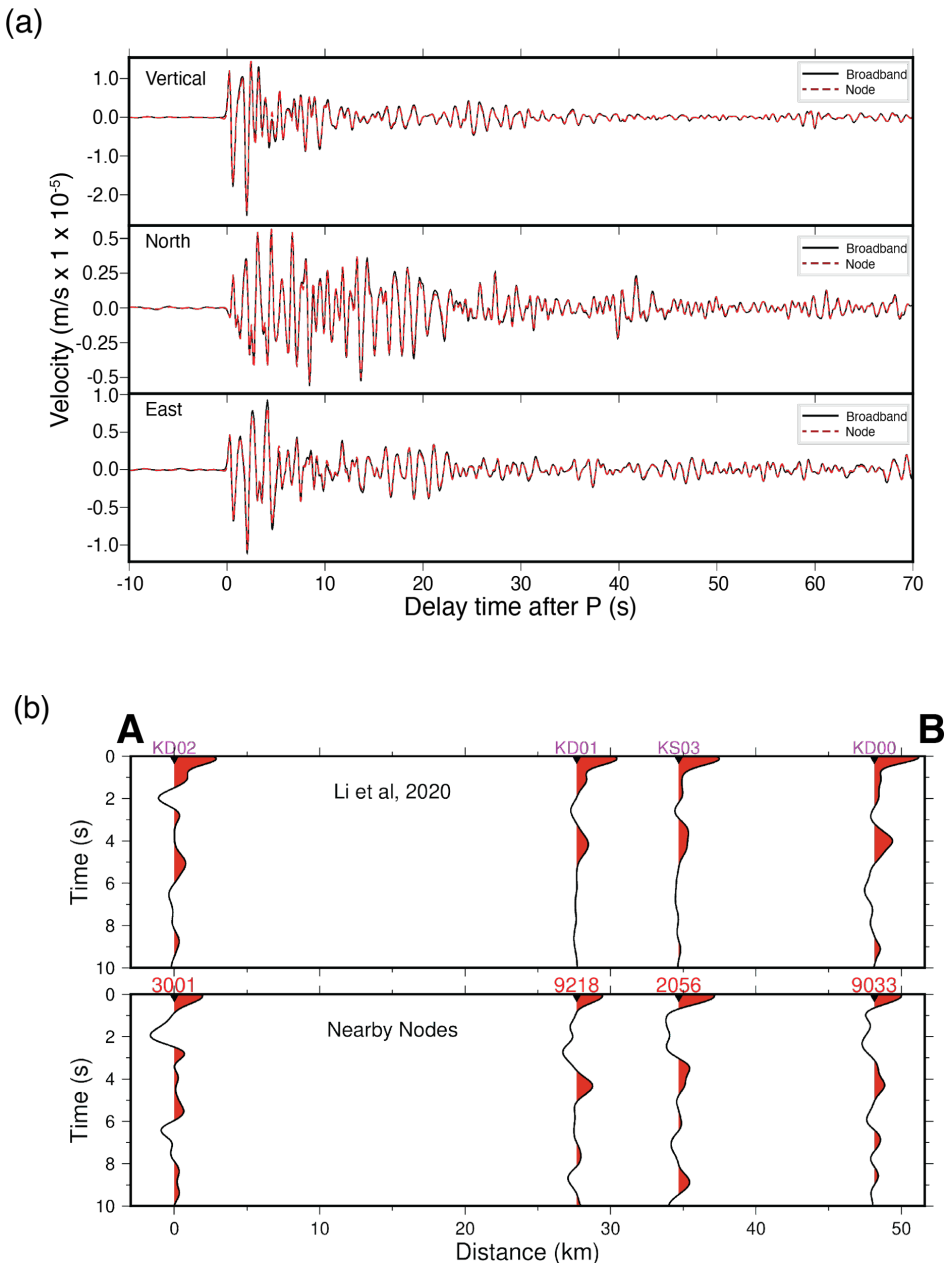

Figure S2. Comparison of near co-located nodal and broadband station waveforms. **(a)** Plots of node station 3001 and broadband station KD02 vertical, east, north component recordings of the 04 June 2019, 04:39:17 UTC Event shown in Figure 2c. **(b)** Plot of the average radial receiver functions for stations KD02, KD01, KS03 and KD00 calculated by Z. Li et al., (2020) projected onto transect AB (top). Plot of the

average radial receiver functions calculated from near-colocated nodal station 3001, 9218, 2056 and 9033 projected onto transect AB.

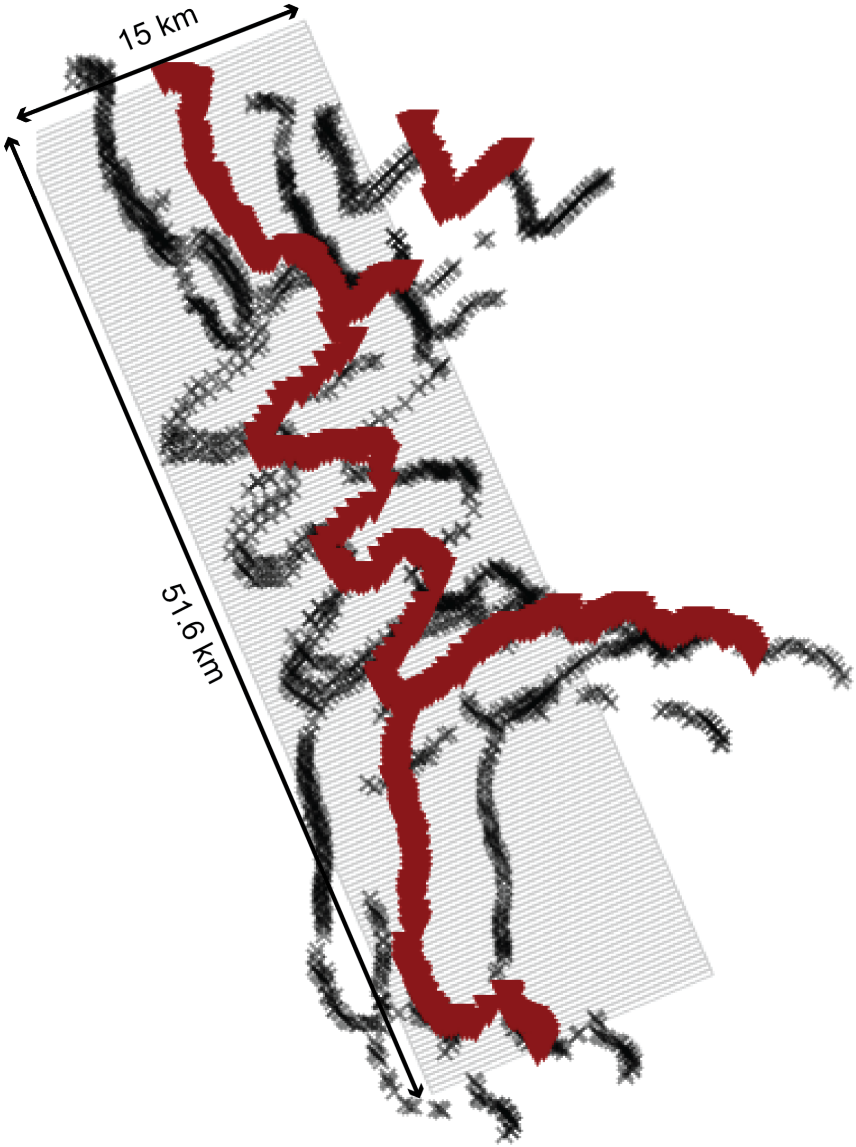

Figure S3. Map of piercing points (black stars) at 20 km depth, and the stations (red inverted triangles) used for common conversion point stacking. The grey rectangles show the position of all the profile boxes used in the stacking.

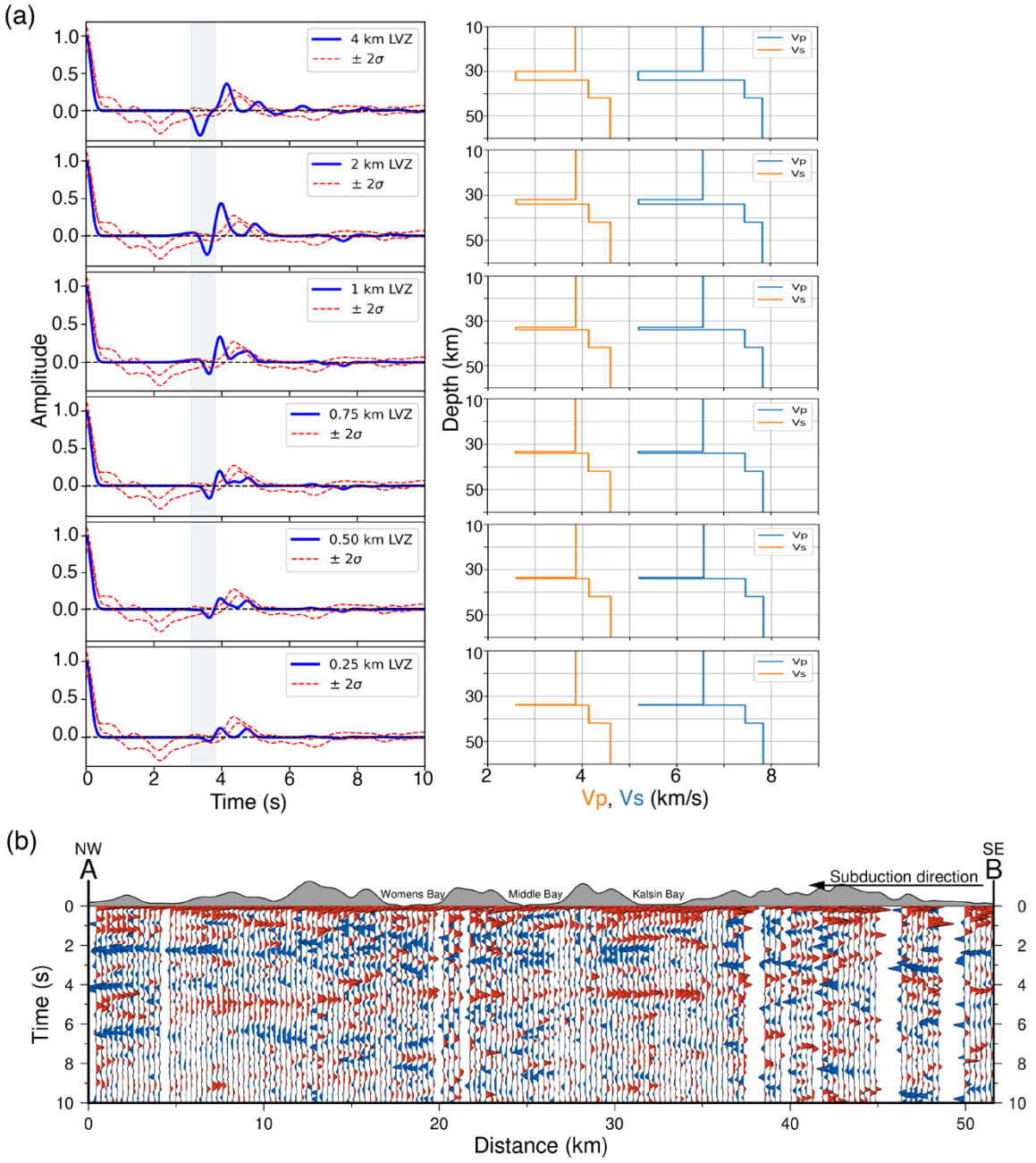

Figure S4. (a) Synthetic tests of 2.5 Hz Ps RFs for models with different LVZ thicknesses. The vertical light blue rectangles in the left panel mark the position of the negative conversion for the 4-km thick LVZ in the top seismogram. The blue lines are synthetic waveforms, and the red dashed lines are the averages of the standard deviations of the field data from Fig.3. **(b)** Moveout-corrected radial receiver functions with a Gaussian value of 10 (~4.8 Hz) stacked by common conversion point.

Time	Latitude	Longitude	Depth	Magnitude
(yyyy/mm/dd hh:mm:ss)	**(°)**	**(°)**	**(km)**	
2019/06/18 13:22:19	38.637	139.4804	12	6.4
2019/06/15 21:56:11	-21.1807	-174.169	13	6.1
2019/06/04 09:46:18	22.8813	121.6704	10	5.6
2019/06/04 04:39:18	29.0623	139.2932	430.3	6.3
2019/06/02 10:36:30	-21.2091	-173.9076	10	6.0
2019/05/26 07:41:15	-5.8132	-75.2775	122.4	8.0
2019/05/30 09:03:29	13.1462	-89.3663	25	6.6

Table S1. Events used in this study.

Model1	V_P **(km/s)**	V_S **(km/s)**	V_P/V_S	**Density (g/cm3)**
Layer1	6.57	3.86	1.7	2.85
Layer2	5.20	2.60	2.0	2.57
Layer3	7.45	4.14	1.8	3.11
Layer4	7.83	4.61	1.7	3.23
Model2	V_P **(km/s)**	V_S **(km/s)**	V_P/V_S	**Density (g/cm3)**
Layer1	6.57	3.75	1.75	2.85
Layer2	7.45	4.14	1.8	3.11
Layer3	7.83	5.22	1.50	3.23
Model3	V_P **(km/s)**	V_S **(km/s)**	V_P/V_S	**Density (g/cm3)**
Layer1	6.57	3.75	1.75	2.85
Layer2	7.83	5.22	1.50	3.23

Table S2. One-Dimensional model parameters.